




Spin-orbit-coupling-driven superfluid states in optical lattices at zero and finite temperaturesKuldeep Suthar ¹, Pardeep Kaur,² Sandeep Gautam ² and Dilip Angom ^{3,4}¹*Institute of Atomic and Molecular Sciences, Academia Sinica, Taipei 10617, Taiwan*²*Indian Institute of Technology Ropar, Rupnagar 140001, Punjab, India*³*Physical Research Laboratory, Ahmedabad 380009, Gujarat, India*⁴*Department of Physics, Manipur University, Canchipur 795003, Manipur, India*

(Received 21 May 2021; revised 30 September 2021; accepted 8 October 2021; published 25 October 2021)

We investigate the quantum phase transitions of a two-dimensional Bose-Hubbard model in the presence of a Rashba spin-orbit coupling with and without thermal fluctuations. The interplay of single-particle hopping, strength of spin-orbit coupling, and interspin interaction leads to superfluid phases with distinct properties. With interspin interactions weaker than intraspin interactions, the spin-orbit coupling induces two finite-momentum superfluid phases. One of them is a phase-twisted superfluid that exists at low hopping strengths and reduces the domain of insulating phases. At comparatively higher hopping strengths, there is a transition from the phase-twisted to a finite-momentum stripe superfluid. With interspin interactions stronger than the intraspin interactions, the system exhibits a phase-twisted to ferromagnetic phase transition. At finite temperatures, the thermal fluctuations destroy the phase-twisted superfluidity and lead to a wide region of normal-fluid states. These findings can be observed in recent quantum gas experiments with spin-orbit coupling in optical lattices.

DOI: [10.1103/PhysRevA.104.043320](https://doi.org/10.1103/PhysRevA.104.043320)**I. INTRODUCTION**

The spin-orbit interaction plays a key role in several areas of condensed matter physics and material science such as topological insulators and superconductors [1–3], quantum Hall effects [4], spin liquids [5], Weyl semimetals [6], and spintronics-based devices [7]. Recent advances in ultracold quantum gas experiments have allowed the implementation of spin-orbit coupling (SOC) and competing interactions in strongly correlated many-body systems [8–10]. These experimental developments afford the possibilities to study novel states of matter, phase transitions, and exotic spin models which are not accessible in conventional condensed matter systems [11,12]. The ultracold atomic systems are ideal platforms for such studies due to the tunability of potentials and multiparticle interactions.

In condensed matter systems, the SOC is an intrinsic property and cannot be tuned [2]. In contrast, it is possible to vary the strength of synthetic SOC in ultracold atoms by tuning the Raman coupling between pseudospin states and thereby different phase transitions can be explored [13–15]. These experiments consider an equal-strength mixture of Rashba and Dresselhaus SOC. However, experimental schemes to realize pure Rashba SOC in ultracold quantum gases have also been proposed [16]. A spin-orbit coupled pseudospin- $\frac{1}{2}$ Bose gas undergoes two successive magnetic phase transitions as the strength of Raman coupling is increased. The first transition is from a stripe to a magnetized plane-wave phase and the second is from the magnetized plane-wave to a nonmagnetic zero-momentum superfluid state for the Raman coupling of the order of the recoil energy [17]. Furthermore, a two-dimensional (2D) SOC exhibits inversion and

C_4 symmetries, thus opening new avenues to study topological band structures and quantum effects. The interaction-driven quantum phase transition and topological region of such a 2D system were explored in a recent experiment [9]. These experimental advances have led to several theoretical studies. Magnetic ordering, such as spin-spiral ordering [18], vortex and skyrmion crystals [12], and ferromagnetic and antiferromagnetic phases [19], has been examined. The effects of the strength and symmetry of SOC on ground-state [20] and crystal momentum distributions [21] and SOC-driven Mott insulator (MI) to superfluid (SF) phase transitions [22] have also been investigated. The strong Rashba SOC destroys the insulating domain and generates finite-momentum and stripe ordered superfluids [12,23,24]. The SOC-driven twisted superfluid states of binary spin mixtures in hexagonal optical lattice have also been observed in a quantum gas experiment [25]. The introduction of optical lattice potential breaks the Galilean invariance [26] and enhances the contrast, lifetime, and parameter regime of the stripe superfluid state [27]. Despite these studies, investigations of the parameter regions of the superfluid states in the spin-orbit coupled Bose-Hubbard model and the effects of thermal fluctuations on the transition between finite-momentum superfluids are lacking. At finite temperatures, the melting of the stripe superfluid phase leads to a wide domain of the stripe normal-fluid (NF) phase [28]. More recently, it has been shown that the SOC leads to the lowering of the critical temperature for the superfluid to NF phase transition and reduces the coherence and spatial orders of magnetic textures [29].

In the present work we study the ground-state phase diagrams of two-component interacting bosons in the presence of Rashba SOC at zero and finite temperatures. We

examine the quantum phase transitions and characterize the SOC-driven finite-momentum superfluid states in two different regimes based on the interspin interactions. For interspin interactions weaker than the intraspin interactions, the two finite-momentum superfluids are phase-twisted (PT) and stripe superfluids, whereas for interspin interactions stronger than intraspin interactions, these are PT and z -polarized ferromagnetic superfluid phases. At $T = 0$ K, the critical hopping of the MI to PT superfluid transition decreases with SOC, which is in agreement with the mean-field predictions. In contrast to the condensed matter systems, the phase diagrams of the system can be explored by tuning the experimental parameters. Furthermore, we extend our study to the case of finite temperature and show the interplay of SOC and thermal fluctuations on the superfluid states. We observe the melting of the PT superfluid state into the insulator and NF phase at finite temperatures.

The paper is structured as follows. We introduce the model Hamiltonian of the present study and provide a brief description of the mean-field Gutzwiller approach in Sec. II. In Sec. III we provide a characterization of the superfluid states of the model considered. In Sec. IV we first discuss the zero-temperature phase diagrams of the Bose-Hubbard model in the presence of synthetic SOC and then we examine the effects of finite temperature on the SOC-driven superfluid states. We summarize in Sec. V.

II. MODEL AND METHOD

We consider a pseudospin system of ultracold bosons loaded into a square optical lattice. The two different atomic hyperfine levels of the same atomic species act as two pseudospin states. The system is well described by a two-component Bose-Hubbard model (BHM) in the presence of Rashba SOC on a 2D optical lattice. The Hamiltonian of the system is [22]

$$\begin{aligned} \hat{H} = & -J \sum_{(i,j)} \hat{\Psi}_i^\dagger \hat{\Psi}_j + \sum_{i,\alpha} (\epsilon_{i\alpha} - \mu) \hat{n}_{i\alpha} \\ & + \frac{1}{2} \sum_{i,\alpha} U_\alpha \hat{n}_{i\alpha} (\hat{n}_{i\alpha} - 1) + U_{\uparrow\downarrow} \sum_i \hat{n}_{i\uparrow} \hat{n}_{i\downarrow} \\ & + i\lambda \sum_{(ij)} \hat{\Psi}_i^\dagger \hat{\mathbf{z}} \cdot (\vec{\sigma} \times \vec{d}_{ij}) \hat{\Psi}_j + \text{H.c.}, \end{aligned} \quad (1)$$

where i is a unique combination of lattice-site indices in two dimensions, i.e., $i \equiv (p, q)$ with p and q site indices in the x and y directions, respectively, and $j \equiv (p', q')$ is a neighboring site of the i th site. Here $\Psi_i = (\hat{b}_{i\uparrow}, \hat{b}_{i\downarrow})^T$ is a two-component bosonic annihilation operator at the i th lattice site, $\alpha = \uparrow, \downarrow$ denotes the pseudospin components, J is the spin-independent hopping amplitude of atoms, and for the present study, we consider equal hopping amplitudes for both components, $\epsilon_{i\alpha}$ is the energy offset of atoms with α spin due to the envelope confining potential and is considered to be zero, μ is the chemical potential, $\hat{n}_{i\alpha} = \hat{b}_{i\alpha}^\dagger \hat{b}_{i\alpha}$ is the number operator, and U_α ($U_{\uparrow\downarrow}$) is the intraspin (interspin) on-site interaction. For the present work, we choose the intraspin interactions to be the same, $U_\uparrow = U_\downarrow = U$. We consider U as the scaling parameter for the tunneling amplitude, chemical potential, interspin

interaction, and energy of the system. The last term represents the SOC generated by Raman lasers which can be tuned in experiments using coherent destructive hopping methods [30] and represents the hopping between neighboring sites with a spin flip. Here λ is the Rashba SOC strength, $\vec{\sigma} = (\sigma_x, \sigma_y, \sigma_z)$ is a vector of Pauli spin matrices, \vec{d}_{ij} is a lattice unit vector between two neighboring sites, and $\hat{\mathbf{z}}$ is a unit vector perpendicular to the lattice plane.

To study the ground-state properties of the system in both strong- and weak-coupling limits, we use the single-site Gutzwiller mean-field (SGMF) theory [31–38]. In this theory, the many-body ground state is the product of single-site states. The Gutzwiller ansatz is

$$|\Psi\rangle = \prod_i |\psi\rangle_i = \prod_i \left(\sum_{n_\uparrow, n_\downarrow}^{N_b} c_{n_\uparrow, n_\downarrow}^i |n_\uparrow, n_\downarrow\rangle_i \right), \quad (2)$$

where $|\psi\rangle_i$ is the single-site ground state and N_b is the number of occupation bases or maximum number of bosons corresponding to each spin state at each lattice site. Here $|n_\uparrow, n_\downarrow\rangle_i$ is the occupation or Fock state, which is the direct product of the occupation states of both spin components, and $c_{n_\uparrow, n_\downarrow}^i$ is the corresponding Gutzwiller coefficient of the coupled Fock state. The SF order parameter and the average occupancy are defined as $\phi_{i\alpha} = \langle \Psi | \hat{b}_{i\alpha} | \Psi \rangle$ and $n_{i\alpha} = \langle \Psi | \hat{n}_{i\alpha} | \Psi \rangle$, respectively. This mean-field approach has been employed in studies of bosons in optical lattices with a synthetic magnetic field and SOC [22, 39–42]. To study the effects of thermal fluctuations at finite temperatures, we use the finite-temperature Gutzwiller theory, and a brief description is presented in the Appendix.

We analyze the system in the weakly interacting limit, where $U_\alpha \ll J$. For this regime, the Hamiltonian (1) in the momentum space can be written as

$$\hat{H}_{\text{kin}} = \sum_{\mathbf{k}} \begin{pmatrix} \hat{b}_{\mathbf{k}\uparrow}^\dagger & \hat{b}_{\mathbf{k}\downarrow}^\dagger \end{pmatrix} \mathcal{H}_{\mathbf{k}} \begin{pmatrix} \hat{b}_{\mathbf{k}\uparrow} \\ \hat{b}_{\mathbf{k}\downarrow} \end{pmatrix}, \quad (3)$$

with

$$\mathcal{H}_{\mathbf{k}} = \begin{pmatrix} -2J(\cos k_x + \cos k_y) & 2i\lambda(\sin k_x - i \sin k_y) \\ -2i\lambda(\sin k_x + i \sin k_y) & -2J(\cos k_x + \cos k_y) \end{pmatrix}.$$

The diagonalization of the above Hamiltonian $\mathcal{H}_{\mathbf{k}}$ yields two energy branches

$$E_{\mathbf{k}\pm} = -2J(\cos k_x + \cos k_y) \pm 2\lambda \sqrt{\sin^2 k_x + \sin^2 k_y}, \quad (4)$$

where $\mathbf{k} = (k_x, k_y)$ and the first term is the spin-independent dispersion relation in a 2D square lattice. The energy spectrum $E_{\mathbf{k}\pm}$ remains invariant under the parity transformation ($k_x \rightarrow -k_x, k_y \rightarrow -k_y$) and permutation of k_x and k_y , ($k_x \rightarrow k_y, k_y \rightarrow k_x$). The noninteracting lowest band structure is shown for two different regimes in Fig. 1. In the absence of SOC ($\lambda = 0$), the lower branch of the band has one minimum at $\mathbf{k} = (0, 0)$. The SOC term modifies the band structure, where the lower branch has four degenerate minima. The presence of SOC breaks the rotational symmetry in \mathbf{k} space and shifts the minima of the lower branch along the diagonals of the first Brillouin zone.

The four degenerate minima in the lower branch are $\mathbf{q}_1 = (k_0, k_0)$, $\mathbf{q}_2 = (-k_0, k_0)$, $\mathbf{q}_3 = (-k_0, -k_0)$, and $\mathbf{q}_4 =$

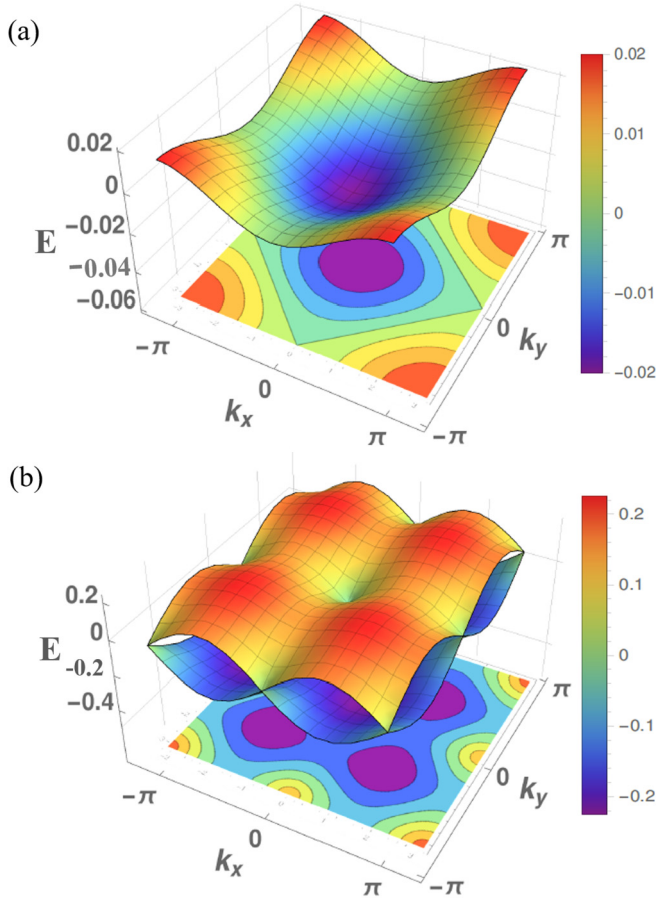


FIG. 1. Noninteracting band structure of the two-dimensional square optical lattice for two regimes. (a) The case $\lambda/J = 0$ represents the single minimum at $\mathbf{k} = 0$ in the absence of SOC. The other case is shown for finite SOC, where the competition between λ and J determines the band structure. (b) For $\lambda/J = 8$, the SOC breaks the rotational symmetry and the minima occur at four finite wave vectors in the lower branch. This is evident from the projection of the lower-energy branch onto the k_x - k_y plane. As λ/J decreases, the minimum of the lower branch tends to approach $\mathbf{k} = 0$.

$(k_0, -k_0)$, where $k_0 = \arctan(\lambda/\sqrt{2}J)$. Hence, the locations of the minima are determined by the strength of SOC.

III. QUANTUM PHASES AND ORDER PARAMETERS

The ground states of ultracold bosons with SOC exhibit insulating and various SF phases. The nature of the SF phase depends on the competition between the single-particle hopping and SOC-induced spin-dependent hopping. At lower J , the incompressible insulating phases are identified by the sum and difference of the expectations of the number operators, $\langle \hat{n}_{\pm} \rangle \equiv \langle \hat{n}_{\uparrow} \rangle \pm \langle \hat{n}_{\downarrow} \rangle$. For the MI phase $\langle \hat{n}_{\pm} \rangle$ is an integer, while the SF phases are characterized by real $\langle \hat{n}_{\pm} \rangle$ and a finite value of the compressibility $\kappa = \partial \langle \hat{n} \rangle / \partial \mu$. In the absence of SOC, the amplitude and phase of the order parameter $\phi_{\uparrow}(\phi_{\downarrow})$ are homogeneous.

Striking features appear when the spin-dependent hopping due to the SOC is finite. This is a complex hopping; it flips the atomic spin while hopping and causes variations in the

phase of SF states. To classify the various SF states which feature distinct phase distributions of the order parameter, we examine the spin-dependent momentum distributions at the wave vector \mathbf{k} ,

$$\langle \rho_{\uparrow, \downarrow}(\mathbf{k}) \rangle = L^{-2} \sum_{i,j} \langle \hat{b}_{i\uparrow}^{\dagger} \hat{b}_{j\downarrow} \rangle e^{i\mathbf{k} \cdot (\mathbf{r}_i - \mathbf{r}_j)}, \quad (5)$$

where L is the system size and \mathbf{r}_i (\mathbf{r}_j) is the location of i th (j th) lattice site. When the interspin interaction is weaker than the intraspin interaction, the SF state can be of three types. (i) The homogeneous superfluid has a uniform amplitude and phase of the order parameter. For this state, the condensation occurs at zero momentum (ZM) and is also referred to as a ZM-SF state. (ii) The phase-twisted superfluid state has an amplitude of $\langle \hat{b}_{i\alpha} \rangle$ that is uniform, but the phase varies diagonally across the lattice. (iii) The stripe (ST) superfluid state has striplike variation in the phase of $\langle \hat{b}_{i\alpha} \rangle$ across the lattice. Thus, we distinguish superfluid states based on their phase variation and momentum distributions. It is worth mentioning that similar SF states have been previously discussed in the continuum where the phases were characterized using the properties of collective excitations [43].

The interplay of spin-dependent hopping (SOC) and single-particle hopping leads to the exotic SF states. We examine the spin-dependent momentum distributions $\langle \rho_{\uparrow, \downarrow}(\mathbf{k}) \rangle$ at $\mathbf{k} = 0$, $\langle \rho_{\uparrow, \downarrow}(\pm k_0, 0) \rangle$, $\langle \rho_{\uparrow, \downarrow}(0, \pm k_0) \rangle$, and $\langle \rho_{\uparrow, \downarrow}(\mathbf{q}_i) \rangle$. Here \mathbf{q}_i and k_0 depend on the ratio of the hopping to the SOC strength, as discussed in Sec. II. For the PT superfluid, the momentum distribution at $\langle \rho_{\uparrow, \downarrow}(\mathbf{q}_i) \rangle$ is finite either at all the \mathbf{q}_i or only at one of the \mathbf{q}_i . This is due to the variation in phase distributions along the diagonal. Hence, this state shows a peak along the diagonal of the Brillouin zone in the \mathbf{k} space. On the other hand, for the ST superfluid states, depending on whether the phase variation is horizontal or vertical, the state exhibits a peak at $\langle \rho_{\uparrow, \downarrow}(\pm k_0, 0) \rangle$ or $\langle \rho_{\uparrow, \downarrow}(0, \pm k_0) \rangle$, respectively. We define $\Phi = \langle \rho_{\uparrow, \downarrow}(k_0, 0) \rangle + \langle \rho_{\uparrow, \downarrow}(-k_0, 0) \rangle + \langle \rho_{\uparrow, \downarrow}(0, k_0) \rangle + \langle \rho_{\uparrow, \downarrow}(0, -k_0) \rangle$, which serves as an order parameter to identify the PT-ST phase transition. Here Φ is zero for the PT superfluid and finite for the ST state. As both PT and ST are SOC-driven finite-momentum superfluid states, $\langle \rho_{\uparrow, \downarrow}(0, 0) \rangle = 0$. In the next section, we characterize the various phase transitions and the finite-momentum superfluids based on the aforementioned classification. Furthermore, when the interspin interaction is strong $U_{\uparrow\downarrow} > 1$, we also report a ferromagnetic phase where the spins orient along the $\pm z$ axis. This is referred to as the z -polarized ferromagnetic (zFM) superfluid state where $\langle \hat{b}_{i\uparrow} \rangle$ ($\langle \hat{b}_{i\downarrow} \rangle$) remains finite and homogeneous but $\langle \hat{b}_{i\downarrow} \rangle$ ($\langle \hat{b}_{i\uparrow} \rangle$) vanishes throughout the lattice. This phase can be easily distinguished from other superfluid states with finite ϕ_{\uparrow} or ϕ_{\downarrow} .

At finite temperatures, the superfluid states are characterized similarly to the case of zero temperature, although the observables are defined with the thermal averages. The definitions of the thermally averaged SF order parameter and occupancy are provided in the Appendix. The normal-fluid state at finite temperatures is identified in the incompressible phases based on the compressibility κ . In the present work, we consider $|n - n_{\text{th}}| \geq 10^{-3}$ as the criterion to identify MI

to NF crossover. Here n and n_{th} are the lattice occupancies at zero and finite temperatures, respectively. Such a criterion has been previously used to distinguish the NF phase of the Bose-Hubbard model at finite temperatures [44].

IV. RESULTS AND DISCUSSION

We study the mean-field ground-state phase diagram of the ultracold bosons and investigate the different SF phases emerging from the competition between the SOC and single-particle hopping. In particular, we examine the system for weak ($U_{\uparrow\downarrow}/U < 1$) and strong ($U_{\uparrow\downarrow}/U > 1$) interspin interactions. We then employ the finite-temperature Gutzwiller theory to probe the effects of thermal fluctuations on the SF phases of the bosons. To generate the phase diagrams, we consider a system size of 8×8 ; the Fock state dimension at each lattice site is $N_b = 6$. The latter is sufficient to represent the quantum phases of the system up to $\mu = 3U$ [31–34]. It is important to note that the initial states play a key role in determining the ground states. We have performed numerical simulations with different initial states and found that a random SF order parameter as the initial state gives the global minimum. The uniform ϕ is not a good choice for the initial state because for some values of the parameters the converged solution corresponds to a local minimum. This is due to the fact that the uniform ϕ do not contribute to the SOC energy as this depends on the relative phase between the ϕ of both pseudospinor components. To obtain the mean-field phase diagrams, we start with a complex random distribution of Gutzwiller coefficients across the lattice and then the corresponding SF order parameter is computed. Hence, our initial state has a random SF order parameter with random amplitude and phase. Our algorithm is based on the self-consistent approach. We diagonalize the single-site Hamiltonians and compute the updated $\phi_{i\alpha}$ at each iteration. This process is repeated until the energy and superfluid order parameter converge up to a tolerance of 10^{-12} . Moreover, we repeat the procedure with 50 random configurations of the initial state to ensure that the ground state has been obtained. We have checked explicitly that the larger number of random configurations does not modify the ground states.

A. Interspin interaction $U_{\uparrow\downarrow} = 0.5$

We first examine the quantum phases of the 2D BHM in the presence of the SOC interaction at zero temperature. The plots in Fig. 2 show the ground-state phase diagrams at different values of the SOC strengths λ with $U_{\uparrow\downarrow} = 0.5U$.

1. No spin-orbit coupling ($\lambda = 0$)

In the absence of SOC, the system supports two quantum phases, the incompressible MI phase and the compressible ZM-SF phase. The MI phase occurs in lobes of different integer commensurate densities. It should be noted that the MI lobes with odd-integer occupancies are smaller than those with even occupancies [45]. As $U_{\uparrow\downarrow}$ increases, the size of the odd-integer Mott lobes grows, whereas even-integer lobes remain the same in size but shift to higher μ/U until $U_{\uparrow\downarrow} = U$. In the absence of SOC, the phase diagram shown in Fig. 2(a)

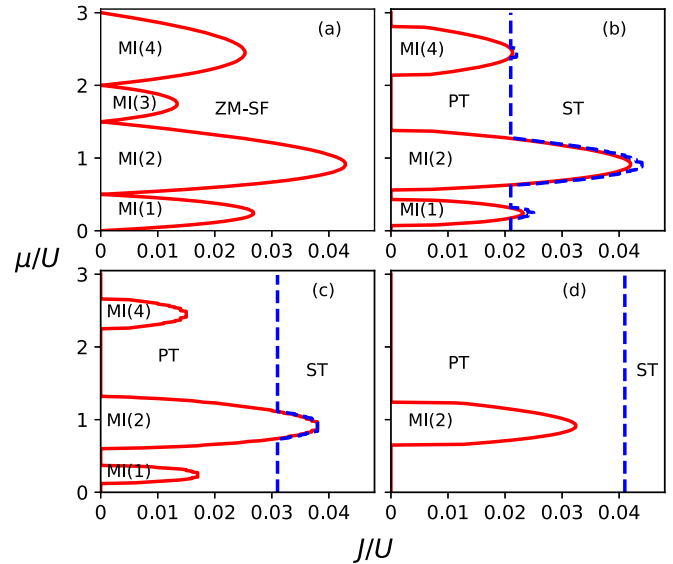


FIG. 2. Zero-temperature ground-state phase diagram in the presence of Rashba SOC for various SOC strengths: (a) $\lambda = 0U$, (b) $\lambda = 0.02U$, (c) $\lambda = 0.03U$, and (d) $\lambda = 0.04U$. The Mott insulator regime is represented by MI(n), where $n = n_{\uparrow} + n_{\downarrow}$ is the total filling or occupancy of the lobe. The interspin interaction $U_{\uparrow\downarrow} = 0.5U$. At $\lambda = 0$, the system exhibits a MI-SF transition, where the SF phase Bose condenses at zero momentum and hence is referred to as the zero-momentum superfluid state. The finite λ results in finite-momentum superfluid phases. Here, as J is varied, the system undergo a PT-ST superfluid phase transition, shown by blue dashed lines. The phase diagrams are obtained using random complex initial states with 50 random configurations. The system size $L = 8 \times 8$ and periodic boundary conditions are considered.

agrees well with previous studies on the two-component BHM [45–48].

2. Finite spin-orbit coupling ($\lambda \neq 0$)

The ground-state phase diagrams for finite SOC are shown in Figs. 2(b)–2(d). Considering the phase diagram at $\lambda = 0.02U$, a prominent feature is the shrinking of the MI lobes. At higher μ , the MI(3) lobe vanishes and is replaced by the SOC-induced SF phase. Thus, even in the atomic limit $J/U = 0$, for certain ranges of μ , the system is in the SF phase due to the SOC. This is evident from the phase diagram in Fig. 2(b), where the SF phase is present at $J/U = 0$ for $\mu/U \leq 0.07$, $0.43 < \mu/U < 0.57$, $1.38 < \mu/U < 2.14$, and $2.8 < \mu/U \leq 3.0$. In the absence of single-particle hopping, i.e., $J = 0$, the superfluidity is due to the transport of atoms in the presence of spin-dependent hopping (SOC). As we increase λ , the MI lobes shrink further and the SF phase is enhanced. For $\lambda = 0.04U$, only the MI(2) lobe survives and the system is in the SOC-generated SF phases in the remaining parameter domain. This is due to the larger region covered by the MI(2) lobe even at $\lambda = 0$. Our computations for larger λ show that the MI(2) lobe also vanishes at $\lambda \approx 0.06U$. Hence, the MI lobe with a larger insulating domain and higher J_c will require larger SOC strengths to result in superfluid states occupying the whole domain of the J/U - μ/U plane. The vanishing of insulating lobes with the formation of SOC-induced

SF states is in agreement with the previous studies [22,24]. Using site-decoupling approximation and second-order perturbation theory, the critical hopping of the MI-SF transition in the presence of SOC is

$$\left(\frac{zJ_c}{U}\right) = \frac{1}{2} \left[\left(\frac{zJ_0}{U}\right) + \sqrt{\left(\frac{zJ_0}{U}\right)^2 - 8\left(\frac{\lambda}{U}\right)^2} \right], \quad (6)$$

where J_0 is the critical hopping of the MI-SF transition in the absence of SOC ($\lambda = 0$). The value of J_0 depends on the occupation number of the species [49]. Here $z = 2d$ is the coordination number of the d -dimensional optical lattice. The value of J_c decreases with λ , which confirms our numerical results in the phase diagrams shown in Fig. 2. As an illustration, for the MI(2)-SF phase transition, the above expression yields values of J_c as 0.0418 and 0.0402 for $\lambda/U = 0.02$ and 0.03, respectively, which are in close agreement with the numerical values in the phase diagrams in Figs. 2(b) and 2(c). Using Eq. (6), the critical SOC strengths where the MI(2) and MI(4) lobes are destroyed are 0.061 and 0.035, respectively, and these are consistent with our numerical results.

At $\lambda = 0$, the only superfluid phase of the system is the ZM superfluid, whereas at a nonzero λ value, it is replaced by finite-momentum superfluids. The nature of superfluid phases near the MI-SF transition can be understood by analyzing the mean-field energies [24]. The hopping energy depends on the relative phase between the same spin state, while the SOC energy depends on the relative phase between different components. For the $\lambda = 0$ case, the minimization of hopping energy leads to a zero phase difference between the states, which corresponds to the ZM superfluid [Fig. 2(a)]. For finite λ , the energies depend on λ/J , relative phases, and the ratio of the amplitudes of ϕ_\downarrow and ϕ_\uparrow . For fixed λ/J and assuming a uniform amplitude of order parameters, the minimization of energies with respect to relative phases corresponds to finite but uniform relative phases [24], which are identified as the PT superfluid state.

The characteristic properties of the finite-momentum and ZM-superfluid states are shown in Fig. 3. The phase variations and the momentum distributions of the finite-momentum superfluids are shown for fixed $\lambda = 0.02U$, $\mu = 1.5U$, and two different J values corresponding to PT and ST superfluids. For the PT superfluid state, the random initial state yields a uniform amplitude and twisted diagonal site variation in the phase, as evident from Fig. 3(a). The phase variation is shown for one of the components, although it should be noted that the other component also follows similar distributions. However, the relative phase of the ϕ between the components is finite, i.e., $\theta_{i\uparrow} \neq \theta_{i\downarrow}$ [24]. In the presence of the interactions, the fourfold symmetry of the lower branch of the lowest-energy band is spontaneously broken. For the PT superfluid phase, the system chooses to be in one of the minima and therefore we observe a single peak at $\mathbf{k} \neq 0$ in the momentum distribution. In particular, the peak in the \mathbf{k} space appears at the diagonal of the Brillouin zone, as represented in Fig. 3(d).

As J is increased, the PT phase undergoes a transition to the ST phase. In the ST superfluid phase obtained with the SGMF approach, the amplitude of $\phi_{i\alpha}$ remains spatially uniform and phase distributions exhibit striplike variation [Fig. 3(b)]. The

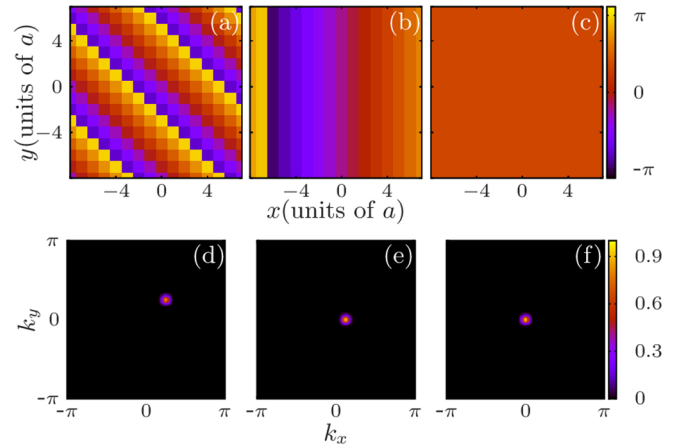


FIG. 3. Lattice-site distributions of the phase variation and spin-dependent momentum distributions of various superfluid states. Phase distributions are represented for (a) PT, (b) ST, and (c) ZM superfluids with (d)–(f) corresponding momentum distributions. The finite-momentum superfluids are obtained using the Gutzwiller mean-field approach for $\lambda = 0.02U$ and $\mu = 1.5U$. The hopping amplitudes in terms of U corresponding to PT and ST superfluids are 0.015 and 0.04, respectively. (c) The ZM superfluid is plotted for $\lambda = 0U$, $\mu = 1.5U$, and $J = 0.04U$. The spatial variation of phase and momentum distributions are shown for one of the components, as the other component also has a similar distribution. The peak in the spin-dependent momentum distributions appears at $\mathbf{k} \neq 0$ for (d) PT and (e) ST states, whereas for (f) ZM superfluid it appears at $\mathbf{k} = 0$. Here a is the lattice constant.

momentum peak is located at $\mathbf{k} \neq 0$ and in particular it lies on the x or y axis, depending on the variation in phase [Fig. 3(e)].

To examine the quantum phase transition between the phase-twisted and the ST superfluid state, we analyze the properties of $\langle \rho_{\uparrow\downarrow}(\mathbf{k}) \rangle$. Since both states are finite-momentum superfluids, the location of their momentum peaks in \mathbf{k} space can serve as an order parameter to identify them. As mentioned earlier in Sec. III, we in particular analyze the evolution of the order parameter Φ , which is the sum of $\langle \rho_{\uparrow\downarrow}(\mathbf{k}) \rangle$ at $\mathbf{k} = (\pm k_0, 0)$ and $(0, \pm k_0)$, as a function of J . For each μ value, we have spanned along the J/U axis, and whenever Φ takes a nonzero value, the critical hopping strength for the PT-ST transition is determined. The error involved in analyzing the phase transition is 10^{-3} , which is the step size (ΔJ) used to span J/U in the numerical computations. Hence, we find that the PT-ST phase transition is sharp. As a representative case, the evolution of Φ at $\mu/U = 1.8$ for three different λ values is shown in Fig. 4. At lower hopping strengths, the ground state is either the MI phase or the finite-momentum PT superfluid and hence Φ remains zero. This is due to the fact that the PT state corresponds to the condensation in $\mathbf{k} = \mathbf{q}_i$ along diagonals of the first Brillouin zone. As J/U increases, a striped ordering of the phase develops with finite Φ , which characterizes the PT-ST superfluid phase transition of the spin-orbit coupled bosons. The critical hopping strength of the PT-ST transition increases as the value of the SOC strength increases. As shown in Fig. 4, the J_c of the PT-ST transition is 0.02, 0.03, and 0.04 for $\lambda = 0.02$, 0.03, and 0.04, respectively. The behavior of Φ and the corresponding transitions for $U_{\uparrow\downarrow} = 0.5$

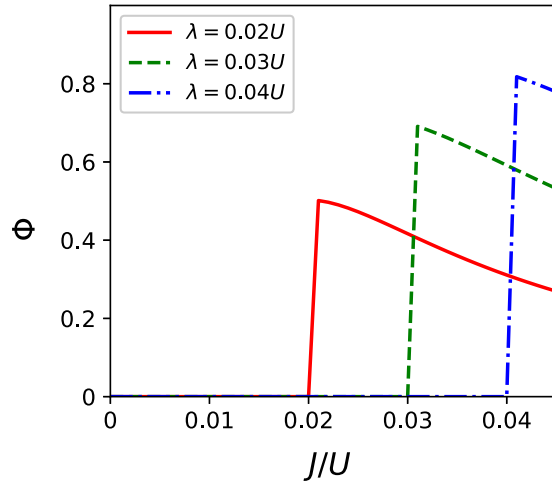


FIG. 4. Evolution of the order parameter Φ , characterizing the finite-momentum PT and ST superfluid states, as a function of the hopping strength J/U . The chemical potential $\mu/U = 1.8$ and interspin interaction $U_{\uparrow\downarrow} = 0.5U$. The Φ is defined in Sec. III. The variation in Φ from zero to finite shows the PT(MI)-ST phase transition.

(Fig. 2) suggest that the PT to ST superfluid phase transition occurs when $\lambda/J \approx 1$. In addition, the PT phase is expected for $\lambda/J \gtrsim 1$, whereas the ST phase appears for $\lambda/J \lesssim 1$. Our computations using random configurations of complex ϕ suggest an increase in J_c as the system size increases. Since the real cold-atom experiments are with the trapped finite-size systems, the transition between finite-momentum superfluids can be observed near the trap center [22].

The SGMF approach fails to capture the density oscillations that should ideally be there in a stripe phase; the reason is that the SGMF approach does not include the intersite atomic correlations. In order to overcome this limitation of the SGMF approach and obtain the nonuniform magnetic ordering and the resulting inhomogeneous superfluidity, one has to use the diagonalization of the cluster of lattice sites as suggested in Ref. [12]. Considering this, we probe the parameter space of the stripe superfluid state obtained from the SGMF theory with the cluster Gutzwiller approach (CGA). The latter improves the intersite correlations and incorporates the effects of the quantum fluctuations. In this approach, the lattice sites are partitioned into a finite number of clusters, where the model terms within the lattice sites of a cluster are treated exactly. A detailed description of the approach is given in our previous works [38,40–42,45]. To examine the parameter domain corresponding to the stripe superfluid, we use a 2×2 cluster and $N_b = 3$. The size of the clusters is sufficient to probe the effects of the atomic correlations on the magnetic ordering of the SOC-driven superfluids. Like in the case of the SGMF approach, sometimes the solution obtained from the CGA is a metastable state corresponding to a local minimum. To avoid this we consider several random configurations of the SF order parameters as the initial states with the CGA and choose the global minimum-energy state as the ground-state phase. The lattice-site distributions of the occupancy, and the amplitude and phase of the SF order parameter are shown in Fig. 5. The profiles are shown for one of the components $|\uparrow\rangle$;

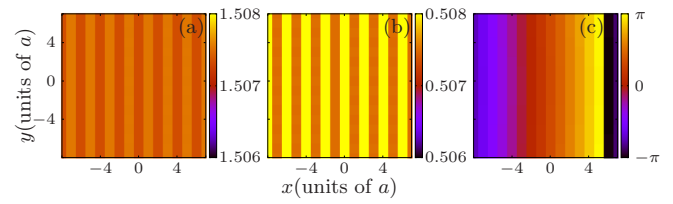


FIG. 5. Lattice-site distributions of the ST_{den} phase obtained using the cluster Gutzwiller approach. The (a) occupancy, (b) amplitude of the order parameter, and (c) phase of a ST_{den} state are shown. The parameters are $\lambda = 0.02U$, $\mu = 1.8U$, and $J = 0.05U$. These distributions are shown for interspin interaction $U_{\uparrow\downarrow} = 0.5U$.

however, the other component also follows similar distributions. We observe stripe variation in the number occupancy $\langle \hat{n}_{i\alpha} \rangle$ and $|\phi_{i\alpha}|$ and hence refer to it as the ST_{den} phase. The amplitudes of the variations remain smaller, which we expect can be enhanced by considering larger clusters of sites.

We further investigate the parameter domain of the stripe superfluid (using the CGA) and find that the ST_{den} phase persists for larger hopping strengths. It continues to the domain where one would get the ZM-SF transition using the SGMF approach. As an example, for the parameters $L = 8 \times 8$, $\lambda = 0.02U$, $\mu = 1.8U$, and $J = 0.1U$, the SGMF theory predicts ZM superfluidity, whereas the CGA gives the ST_{den} phase for these parameters. Hence, the latter extends the parameter space of the ST_{den} phase by taking into account the quantum correlations. This suggests the applicability of the SGMF theory to describe the quantum phase transitions usually for $J/U \rightarrow 0$ [12,22,24]. Therefore, in the present work, we investigate the phase transitions in the range from $J = 0$ to $J \approx 0.08U$. The stability of the ST_{den} superfluid in a wider parameter regime is consistent with the observation of this state in the presence of a weak lattice potential in a recent experiment [27]. In the present work, the CGA is used to ascertain the nature of the ST and ZM phases obtained from the SGMF approach. However, a detailed analysis of the phase diagrams with the CGA is left for future work.

B. Interspin interaction $U_{\uparrow\downarrow} = 1.5$

Here we discuss the quantum phases generated due to the effects of SOC when the interspin interaction is stronger than the intraspin ones ($U_{\uparrow\downarrow}/U > 1$). In this parameter regime, we first review the phase diagram of the two-component interacting bosonic system in the absence of SOC. The phase diagram for $U_{\uparrow\downarrow} = 1.5U$ at $\lambda = 0$ is shown in Fig. 6(a). Above the phase separation criterion, at $J = 0$, the width of all MI lobes is $\Delta\mu/U = 1$. Moreover, the critical hopping of the MI(1)-SF transition in Fig. 6(a) becomes identical to the MI(2)-SF for the $U_{\uparrow\downarrow} < U$ case as shown in Fig. 2(a). Details of the quantum phase transitions as a function of $U_{\uparrow\downarrow}$ for the two-component interacting scalar-bosonic system were reported in our previous study [45]. In the phase-separated superfluid, the condensation occurs in one of the components only and it resembles the zFM phase [12,29]. We further examine the SOC-driven superfluid phases and their parameter space as λ is varied. The phase diagrams for three representative cases are shown in Figs. 6(b)–6(d). At $\lambda = 0.02U$, for lower

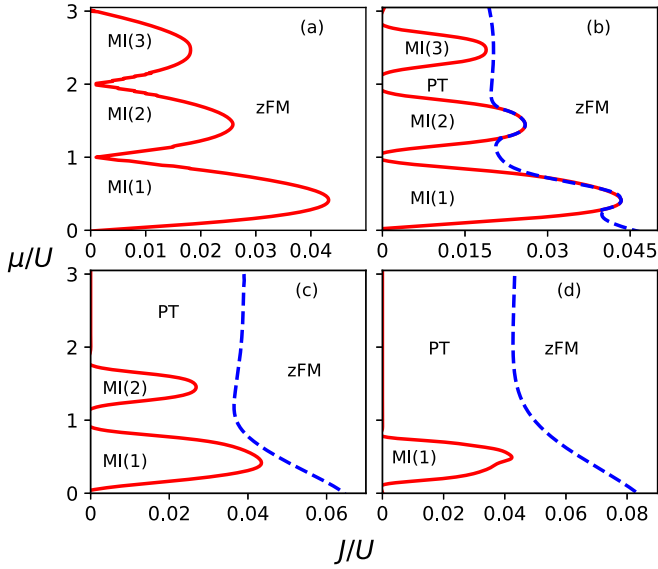


FIG. 6. Zero-temperature ground-state phase diagram in the presence of Rashba SOC for various SOC strengths: (a) $\lambda = 0U$, (b) $\lambda = 0.02U$, (c) $\lambda = 0.03U$, and (d) $\lambda = 0.04U$. The filling or occupancy of the Mott lobe is represented by n in $MI(n)$. The interspin interaction $U_{\uparrow\downarrow} = 1.5U$. The superfluidity near the MI lobes is twisted in character, while at higher J the system is in the zFM state.

hopping strengths, the phase-modulated PT superfluid emerges between the insulating lobes as shown in Fig. 6(b). For the phase-separated regime, the uniform occupancy of the PT state is observed for $n_i = n_{i\uparrow} + n_{i\downarrow}$ and the phase of each component varies diagonally as shown in Fig. 3(a). A further increase in J results in a transition to the zFM superfluid. The effects of SOC at higher strengths $\lambda = 0.03U$ and $0.04U$ are shown in Figs. 6(c) and 6(d), respectively. At $\lambda = 0.03U$, the MI(3) completely vanishes and the parameter regime of the PT superfluid phase is enhanced. This is also evident from the SF region between the MI(1) and MI(2) lobes. At $\lambda = 0.04U$, the destruction of Mott lobes is enhanced as indicated by the absence of MI(2). As SOC strength increases, the melting of insulating lobes occurs first for higher-density lobes and then it continues to the lower-density ones. In addition, the J_c of the MI-SF transition also decreases with λ . We find that at higher $\lambda \approx 0.065U$, the MI(1) phase gets completely destroyed and the system exhibits a superfluid phase transition between PT and zFM states. The transition between the PT and zFM states is a broad one. To get the phase boundary for this transition, we use a nonlinear least-squares fitting and the residual is of the order of 10^{-3} . It is important to note that for stronger interspin interaction $U_{\uparrow\downarrow}/U > 1$, we do not observe the ST phase. This is consistent with the quantum phases of the continuum system with SOC where the tuning of Raman coupling for a strong interspin interaction does not lead to the ST phase [43].

C. Finite-temperature results for $U_{\uparrow\downarrow} = 0.5$

At finite temperature, the Mott lobe melts into the NF phase due to thermal fluctuations. The NF phase has no long-

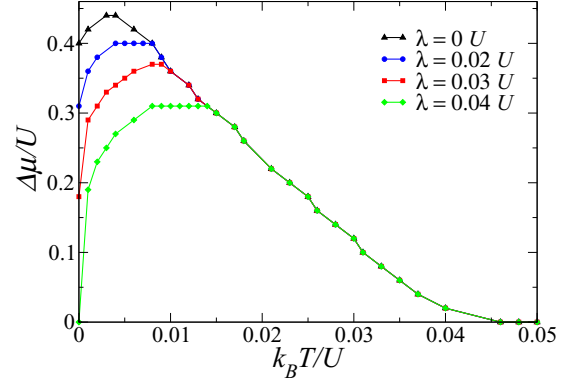


FIG. 7. Width of the first Mott lobe $MI(1)$ at $J = 0.01U$ as a function of temperature for various SOC strengths. The values of λ in units of U are shown in the legend. Here the interspin interaction $U_{\uparrow\downarrow} = 0.5U$. At lower temperatures, the melting of the MI lobe depends on the value of λ , and at higher $k_B T$ the width remains similar to the $\lambda = 0$ case. For all cases, with and without SOC, the $MI(1)$ phase completely melts and replaced by NF phase at $k_B T/U \approx 0.046$.

range order, but it is compressible ($\kappa \neq 0$). Therefore, this phase can be distinguished from the insulating MI phases by finite κ . We examine the melting of the MI phase as a function of temperature for various SOC strengths. In Fig. 7 we plot the width of the first Mott lobe $MI(1)$ at $J = 0.01U$ for different values of λ . For $\lambda = 0$, at lower temperatures, the width of the MI lobe first increases for $k_B T/U < 0.004$.

At $k_B T/U \approx 0.004$ the Mott lobe starts melting and the width of the lobe decreases with temperature. At $k_B T/U \approx 0.046$, the MI phase is completely replaced by the NF phase. However, for finite λ there is a combined effect of SOC and finite temperature on the width of the Mott lobe. For $\lambda = 0.02U$, at low temperatures the width first increases and then at $k_B T/U \approx 0.009$ the thermal fluctuations overcome the SOC effects; this leads to a decrease in the width. The effects of SOC are prominent at larger values of λ , as evident for the $\lambda = 0.03U$ and $0.04U$ cases in Fig. 7. At higher temperatures, the melting of the MI phase is independent of λ and the decrease in the width of the MI lobe is similar to the $\lambda = 0$ case.

We further discuss the finite-temperature phase diagram at $k_B T/U = 0.03$, shown in Fig. 8. At $\lambda = 0$, the thermal fluctuations destroy the off-diagonal long-range order of the SF phase and extend the parameter space of the NF phase. Odd Mott lobes stretch along the J/U axis. For example, at $k_B T = 0$, the critical hopping of the $MI(1)$ -SF transition is 0.0268 in Fig. 2(a) and at $k_B T/U = 0.03$ it increases to 0.0422 , as evident from Fig. 8(a). Similar enhancement is also apparent for $MI(3)$ from a comparison of Figs. 8(a) and 2(a). In the presence of SOC, there is an interplay of the effects of SOC and finite temperature. For smaller SOC strengths ($\lambda = 0.02$ and 0.03), the remarkable feature of the reemergence of MI lobes at the cost of finite-momentum superfluids at finite temperature is observed. In particular, the SOC-induced PT phase near the atomic limit in Fig 2(b) melts into $MI(3)$ and NF phases as shown in Fig. 8(b). The destruction of PT superfluidity in a wide region of the NF state

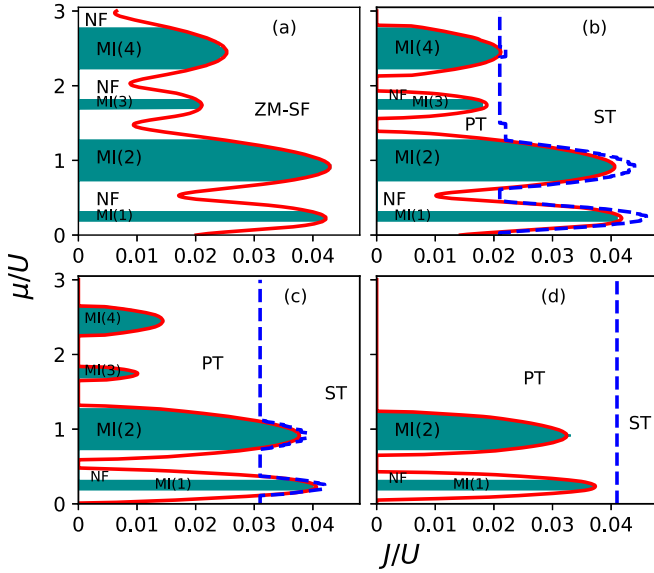


FIG. 8. Finite-temperature phase diagram of the BHM for different values of λ at $k_B T/U = 0.03$: (a) $\lambda = 0U$, (b) $\lambda = 0.02U$, (c) $\lambda = 0.03U$, and (d) $\lambda = 0.04U$. The interspin interaction $U_{\uparrow\downarrow} = 0.5U$. The shaded green bands are the insulating MI regions which are distinguished from the NF phase present at finite T . The reemergence of insulating regimes and destruction of PT superfluidity at finite temperatures are observed. The constant width of MI(1) for both zero and finite SOC confirms the behavior reported in Fig. 7. The blue dashed line represents the PT-ST superfluid phase transition obtained using the finite-temperature Gutzwiller mean-field approach.

at finite temperatures is consistent with the previous Monte Carlo study of strongly correlated bosons with SOC [28]. The reemergence of insulating domains at finite temperature is in agreement with our analysis of the width of the MI lobe with SOC, which is shown in Fig. 7. While increasing the SOC strengths from 0.02 [Fig. 8(b)] to 0.03 [Fig. 8(c)], the PT state is favored by melting the NF and MI phases. At $\lambda = 0.04U$, the phase boundary of the PT to ST superfluid transition, as in the case of zero temperature, remains unchanged and independent of the average particle densities or μ at finite temperatures.

D. Finite-temperature results for $U_{\uparrow\downarrow} = 1.5$

Like in the case of $U_{\uparrow\downarrow} = 0.5U$, we examine the finite-temperature phase diagram in the phase-separated regime with SOC. In particular, we explore the stability of the finite-momentum superfluids with the thermal fluctuations arising from finite T . To gain additional insight, we briefly review the $\lambda = 0$ case. As expected, the insulating lobes melt to the NF phase at $k_B T/U = 0.03$, which is discernible from the phase diagram shown in Fig. 9(a). The phase diagrams of $\lambda \neq 0$ at $k_B T/U = 0.03$ are shown in Figs. 9(b)–9(d). At $\lambda = 0.02U$, the thermal fluctuations favor the insulating domains, and the emergence of the NF phase between the MI lobes reduces the PT superfluidity, as is evident from a comparison of Fig. 9(b) with Fig. 6(b). The reemergence of MI lobes at finite T is also seen in this case, as can be confirmed by comparing Figs. 9(c) and 9(d) with Figs. 6(c) and 6(d). At

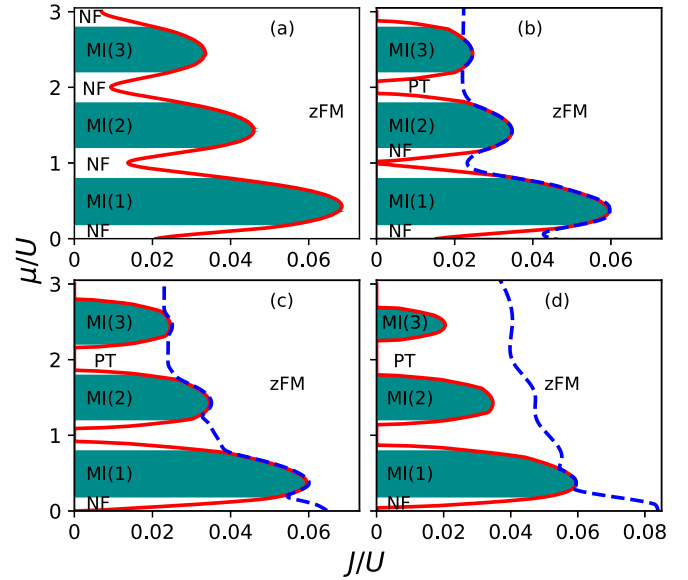


FIG. 9. Finite-temperature phase diagram of the BHM for different values of SOC strengths at $U_{\uparrow\downarrow} = 1.5U$: (a) $\lambda = 0.02U$, (b) $\lambda = 0.03U$, and (c) $\lambda = 0.04U$. The shaded green bands represent the residual insulating domains in the presence of thermal fluctuations. Outside the bands tiny white regions show the NF phase. The thermal energy corresponding to temperature is $k_B T/U = 0.03$. The finite temperature stabilizes the MI phases against the SOC and suppresses the finite-momentum superfluidity. This is evident from (c) and (d), as compared to the corresponding zero-temperature case shown in Figs. 6(c) and 6(d).

the phase boundaries, the critical hopping of the MI-zFM and PT-zFM transitions is shifted to higher J at finite temperature as compared to the critical J at zero temperature. The effect of the increase in SOC strength leading to the increase in the PT superfluid phase is also evident in the phase diagrams shown in Figs. 9(c) and 9(d) which are similar to $U_{\uparrow\downarrow}/U < 1$ case.

V. CONCLUSION

We have studied the parameter domain of various finite-momentum superfluids of spin-orbit-coupled ultracold bosonic atoms in two-dimensional optical lattices. To examine various superfluid states with different atomic densities and phase ordering, we have used spin-dependent momentum distributions, a routinely measured observable in cold-atom experiments. For $U_{\uparrow\downarrow} < U$, with $\lambda/J \gtrsim 1$ the favored superfluid phase is the PT phase, whereas with $\lambda/J \lesssim 1$ the system is in the ST phase. Starting with the PT phase, the increase in J results in the PT to ST superfluid phase transition. We have shown that the inclusion of the quantum fluctuations via the cluster Gutzwiller approach results in the ST_{den} phase corresponding to the parameter domain of the ST phase obtained with the Gutzwiller mean-field theory. In the limit $U_{\uparrow\downarrow} > U$, the stripe superfluid is absent and the phase-twisted to z -polarized ferromagnetic transition is observed as J is varied. We have further shown that the thermal fluctuations destroy the phase-twisted superfluidity and favor the insulating and normal states. The results of the present study are pertinent

to the ongoing quantum gas experiments with spin-orbit coupling and offer a parameter space in the J - μ plane to observe the finite-momentum superfluids.

ACKNOWLEDGMENTS

We thank Deepak Gaur and Hrushikesh Sable for valuable discussions and acknowledge the support of High Performance Computing Cluster at IAMS, Academia Sinica, Taiwan. S.G. thanks Science and Engineering Research Board, Department of Science and Technology, Government of India (Project No. ECR/2017/001436) for support.

APPENDIX: FINITE-TEMPERATURE GUTZWILLER MEAN-FIELD THEORY

We incorporate the effects of the thermal fluctuations at finite temperatures by considering the thermal average of the observable quantities. To compute the thermal average, we first get the full set of eigenspectra obtained from the diagonalization of the mean-field Hamiltonian. We further use the single-site energy spectrum E_i^l and the eigenstates $|\psi\rangle_i^l$ to evaluate the partition function of the system

$$Z_i = \sum_{l=1}^{N_b} e^{-\beta E_i^l}, \quad (\text{A1})$$

where l is the eigenstate index, N_b is the Fock space dimension, $\beta = (k_B T)^{-1}$, and T is the temperature of the system. At finite T , the region of the phase diagram with a vanishing SF order parameter and the real number occupancy $\langle \hat{n}_{i\alpha} \rangle$ is defined as the normal-fluid state.

From the definition of the partition function, the thermal average of the SF order parameter is

$$\langle \phi_{i\alpha} \rangle = \frac{1}{Z_i} \sum_{l=0}^{N_b} \langle \psi | \hat{b}_{i\alpha} e^{-\beta E_i^l} | \psi \rangle_i^l, \quad (\text{A2})$$

where $\alpha = \uparrow, \downarrow$ is the spin-component index and $\langle \dots \rangle$ represents the thermal averaging of ϕ . Similarly, the atomic occupancy at finite T is defined as

$$\langle \langle \hat{n}_{i\alpha} \rangle \rangle = \frac{1}{Z_i} \sum_{l=0}^{N_b} \langle \psi | \hat{n}_{i\alpha} e^{-\beta E_i^l} | \psi \rangle_i^l. \quad (\text{A3})$$

The average occupancy is $\langle n_\alpha \rangle = \sum_i \langle \langle \hat{n}_{i\alpha} \rangle \rangle / L$. At finite T , the spin-dependent momentum distributions $\langle \rho_{\uparrow, \downarrow}(\mathbf{k}) \rangle$ are computed from the thermally averaged SF order parameters.

-
- [1] M. Z. Hasan and C. L. Kane, *Rev. Mod. Phys.* **82**, 3045 (2010).
 [2] X.-L. Qi and S.-C. Zhang, *Rev. Mod. Phys.* **83**, 1057 (2011).
 [3] A. Manchon, H. C. Koo, J. Nitta, S. M. Frolov, and R. A. Duine, *Nat. Mater.* **14**, 871 (2015).
 [4] Z. F. Ezawa, *Quantum Hall Effects: Recent Theoretical and Experimental Developments*, 3rd ed. (World Scientific, Singapore, 2013).
 [5] L. Balents, *Nature (London)* **464**, 199 (2010).
 [6] X. Wan, A. M. Turner, A. Vishwanath, and S. Y. Savrasov, *Phys. Rev. B* **83**, 205101 (2011).
 [7] I. Žutić, J. Fabian, and S. Das Sarma, *Rev. Mod. Phys.* **76**, 323 (2004).
 [8] Z. Wu, L. Zhang, W. Sun, X.-T. Xu, B.-Z. Wang, S.-C. Ji, Y. Deng, S. Chen, X.-J. Liu, and J.-W. Pan, *Science* **354**, 83 (2016).
 [9] W. Sun, B.-Z. Wang, X.-T. Xu, C.-R. Yi, L. Zhang, Z. Wu, Y. Deng, X.-J. Liu, S. Chen, and J.-W. Pan, *Phys. Rev. Lett.* **121**, 150401 (2018).
 [10] S. Zhang and G.-B. Jo, *J. Phys. Chem. Solids* **128**, 75 (2019).
 [11] J. Radić, A. Di Ciolo, K. Sun, and V. Galitski, *Phys. Rev. Lett.* **109**, 085303 (2012).
 [12] W. S. Cole, S. Zhang, A. Paramekanti, and N. Trivedi, *Phys. Rev. Lett.* **109**, 085302 (2012).
 [13] Y.-J. Lin, K. Jiménez-García, and I. B. Spielman, *Nature (London)* **471**, 83 (2011).
 [14] J. Li, W. Huang, B. Shteynas, S. Burchesky, F. Ç. Top, E. Su, J. Lee, A. O. Jamison, and W. Ketterle, *Phys. Rev. Lett.* **117**, 185301 (2016).
 [15] J.-R. Li, J. Lee, W. Huang, S. Burchesky, B. Shteynas, F. Ç. Top, A. O. Jamison, and W. Ketterle, *Nature (London)* **543**, 91 (2017).
 [16] V. Galitski and I. B. Spielman, *Nature (London)* **494**, 49 (2013).
 [17] S.-C. Ji, J.-Y. Zhang, L. Zhang, Z.-D. Du, W. Zheng, Y.-J. Deng, H. Zhai, S. Chen, and J.-W. Pan, *Nat. Phys.* **10**, 314 (2014).
 [18] Z. Cai, X. Zhou, and C. Wu, *Phys. Rev. A* **85**, 061605(R) (2012).
 [19] M. Gong, Y. Qian, M. Yan, V. W. Scarola, and C. Zhang, *Sci. Rep.* **5**, 10050 (2015).
 [20] A. T. Bolukbasi and M. Iskin, *Phys. Rev. A* **89**, 043603 (2014).
 [21] D. Yamamoto, I. B. Spielman, and C. A. R. Sá de Melo, *Phys. Rev. A* **96**, 061603(R) (2017).
 [22] M. Yan, Y. Qian, H.-Y. Hui, M. Gong, C. Zhang, and V. W. Scarola, *Phys. Rev. A* **96**, 053619 (2017).
 [23] T. Groß, K. Saha, K. Sengupta, and M. Lewenstein, *Phys. Rev. A* **84**, 053632 (2011).
 [24] S. Mandal, K. Saha, and K. Sengupta, *Phys. Rev. B* **86**, 155101 (2012).
 [25] P. Soltan-Panahi, D.-S. Luhmann, J. Struck, P. Windpassinger, and K. Sengstock, *Nat. Phys.* **8**, 71 (2012).
 [26] C. Hamner, Y. Zhang, M. A. Khamehchi, M. J. Davis, and P. Engels, *Phys. Rev. Lett.* **114**, 070401 (2015).
 [27] T. M. Bersano, J. Hou, S. Mossman, V. Gokhroo, X.-W. Luo, K. Sun, C. Zhang, and P. Engels, *Phys. Rev. A* **99**, 051602(R) (2019).
 [28] C. Hickey and A. Paramekanti, *Phys. Rev. Lett.* **113**, 265302 (2014).
 [29] A. Dutta, A. Joshi, K. Sengupta, and P. Majumdar, *Phys. Rev. B* **99**, 195126 (2019).
 [30] Y. Zhang, G. Chen, and C. Zhang, *Sci. Rep.* **3**, 1937 (2013).
 [31] M. C. Gutzwiller, *Phys. Rev. Lett.* **10**, 159 (1963).
 [32] D. S. Rokhsar and B. G. Kotliar, *Phys. Rev. B* **44**, 10328 (1991).
 [33] W. Krauth, M. Caffarel, and J.-P. Bouchaud, *Phys. Rev. B* **45**, 3137 (1992).

- [34] K. Sheshadri, H. R. Krishnamurthy, R. Pandit, and T. V. Ramakrishnan, *Europhys. Lett.* **22**, 257 (1993).
- [35] C. Menotti, C. Trefzger, and M. Lewenstein, *Phys. Rev. Lett.* **98**, 235301 (2007).
- [36] M. Iskin, *Phys. Rev. A* **83**, 051606(R) (2011).
- [37] S. Bandyopadhyay, R. Bai, S. Pal, K. Suthar, R. Nath, and D. Angom, *Phys. Rev. A* **100**, 053623 (2019).
- [38] K. Suthar, R. Kraus, H. Sable, D. Angom, G. Morigi, and J. Zakrzewski, *Phys. Rev. B* **102**, 214503 (2020).
- [39] Y. Kuno, K. Shimizu, and I. Ichinose, *Phys. Rev. A* **95**, 013607 (2017).
- [40] R. Bai, S. Bandyopadhyay, S. Pal, K. Suthar, and D. Angom, *Phys. Rev. A* **98**, 023606 (2018).
- [41] S. Pal, R. Bai, S. Bandyopadhyay, K. Suthar, and D. Angom, *Phys. Rev. A* **99**, 053610 (2019).
- [42] K. Suthar, H. Sable, R. Bai, S. Bandyopadhyay, S. Pal, and D. Angom, *Phys. Rev. A* **102**, 013320 (2020).
- [43] L. Chen, H. Pu, Z.-Q. Yu, and Y. Zhang, *Phys. Rev. A* **95**, 033616 (2017).
- [44] P. Buonsante and A. Vezzani, *Phys. Rev. A* **70**, 033608 (2004).
- [45] R. Bai, D. Gaur, H. Sable, S. Bandyopadhyay, K. Suthar, and D. Angom, *Phys. Rev. A* **102**, 043309 (2020).
- [46] D. Yamamoto, T. Ozaki, C. A. R. Sá de Melo, and I. Danshita, *J. Low Temp. Phys.* **175**, 258 (2013).
- [47] D. Yamamoto, T. Ozaki, C. A. R. Sá de Melo, and I. Danshita, *Phys. Rev. A* **88**, 033624 (2013).
- [48] Y. Kato, D. Yamamoto, and I. Danshita, *Phys. Rev. Lett.* **112**, 055301 (2014).
- [49] G.-H. Chen and Y.-S. Wu, *Phys. Rev. A* **67**, 013606 (2003).